Solutal Marangoni effect determines bubble dynamics during electrocatalytic hydrogen evolution

Park, S; Liu, L.; Demirkır, Ç.; Heijden, O. van der; Lohse, D.; Krug, D.; Koper, M.T.M.

nature chemistry

Article

https://doi.org/10.1038/s41557-023-01294-y

Solutal Marangoni effect determines bubble dynamics during electrocatalytic hydrogen evolution

Received: 10 February 2023

Accepted: 14 July 2023

Published online: 10 August 2023

Check for updates

Sunghak Park[1], Luhao Liu[2], Çayan Demirkır[2], Onno van der Heijden[1], Detlef Lohse[2,3], Dominik Krug[2] ✉ & Marc T. M. Koper[1] ✉

Understanding and manipulating gas bubble evolution during electrochemical water splitting is a crucial strategy for optimizing the electrode/electrolyte/gas bubble interface. Here gas bubble dynamics are investigated during the hydrogen evolution reaction on a well-defined platinum microelectrode by varying the electrolyte composition. We find that the microbubble coalescence efficiency follows the Hofmeister series of anions in the electrolyte. This dependency yields very different types of H_2 gas bubble evolution in different electrolytes, ranging from periodic detachment of a single H_2 gas bubble in sulfuric acid to aperiodic detachment of small H_2 gas bubbles in perchloric acid. Our results indicate that the solutal Marangoni convection, induced by the anion concentration gradient developing during the reaction, plays a critical role at practical current density conditions. The resulting Marangoni force on the H_2 gas bubble and the bubble departure diameter therefore depend on how surface tension varies with concentration for different electrolytes. This insight provides new avenues for controlling bubble dynamics during electrochemical gas bubble formation.

Hydrogen is one of the most promising energy carriers for a future sustainable energy system[1,2]. Electrochemical water splitting with renewable electricity is a scalable technology that can provide clean hydrogen in a sustainable way without greenhouse gas emissions[3]. In electrochemical water splitting, hydrogen (H_2) gas is formed through the hydrogen evolution reaction (HER) at the cathode, and oxygen (O_2) gas is formed through the oxygen evolution reaction at the anode[4,5]. Under practical high-current-density operating conditions, gas bubbles form at each electrified electrode/electrolyte interface due to the high local concentration of gaseous products. Therefore, a detailed understanding of the various processes at the electrode/electrolyte/gas bubble interface and of the mechanisms affecting transport is crucial for optimizing electrochemical water splitting performance. To achieve such an understanding, the descriptor-based volcano plot has been successfully used as a framework for designing electrode materials for optimal activity[6]. More recently, many efforts have been devoted to assessing the effect of the electrolyte on atomic- and molecular-level processes, including the role of local water structure, cations and anions[7–12]. In the case of gas bubble formation, it has been known that gas bubbles affect gas-evolving electrochemical systems in various respects, including changing the gas concentration profile[13,14], reducing the surface area due to adherent bubbles[15], increasing ohmic resistance[16] and enhancing mass transport[17]. In addition, controlling surface wettability has provided improved activities through facile gas bubble detachment[18]. However, a more detailed understanding of electrochemically generated gas bubble dynamics and its intricate dependencies on electrochemical phenomena have been receiving less attention[19].

[1]Leiden Institute of Chemistry, Leiden University, Leiden, the Netherlands. [2]Physics of Fluids Group, Max Planck Center Twente for Complex Fluid Dynamics, Faculty of Science and Technology, University of Twente, Enschede, the Netherlands. [3]Max Planck Institute for Dynamics and Self-Organization, Göttingen, Germany. ✉e-mail: d.j.krug@utwente.nl; m.koper@lic.leidenuniv.nl

https://doi.org/10.1038/s41557-023-01294-y

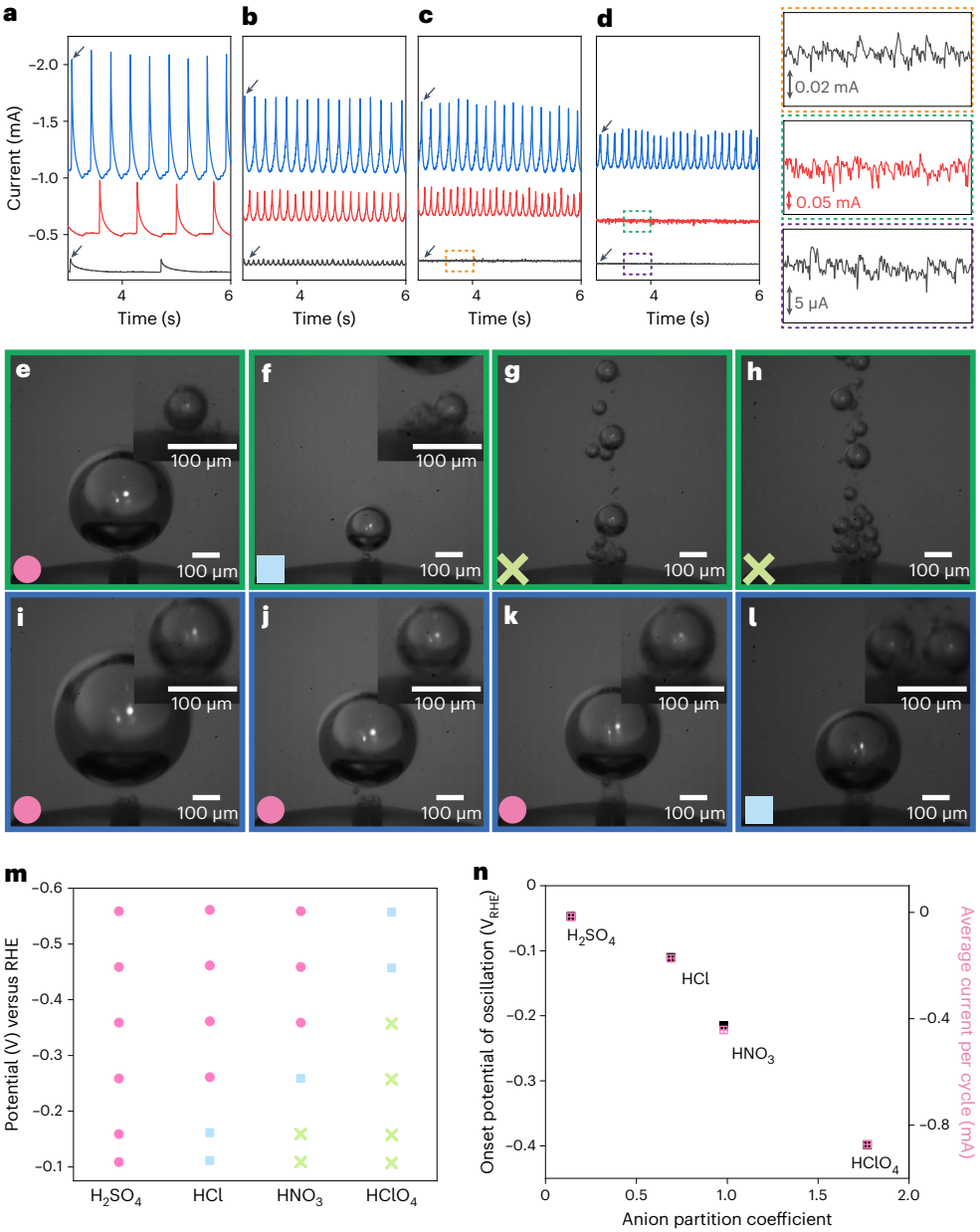

Fig. 1 | Anion effects on HER current oscillation and H_2 gas bubble evolution. **a**–**d**, Chronoamperometry measurements at −0.56 V_{RHE} (blue curves), −0.36 V_{RHE} (red curves), −0.16 V_{RHE} (black curves) in 1 M H_2SO_4 (**a**), 1 M HCl (**b**), 1 M HNO_3 (**c**) and 1 M $HClO_4$ (**d**). Graphs shown on the right are enlargements of the orange, green and purple dotted boxes. **e**–**l**, Snap images of different H_2 gas bubble detachment moments during chronoamperometry (indicated by the black arrows in **a**–**d**) in 1 M H_2SO_4 (**e**,**i**), 1 M HCl (**f**,**j**), 1 M HNO_3 (**g**,**k**) and 1 M $HClO_4$ (**h**,**l**). Images in green and blue boxes were obtained during chronoamperometry at −0.16 V_{RHE} (**e**,**f**,**g**,**h**) and −0.56 V_{RHE} (**i**,**j**,**k**,**l**). Insets: images taken at $\Delta t = 4$ ms after detachment. Circles, periodic formation and detachment of a single H_2 gas bubble that forms within 4 ms. Squares, periodic formation and detachment of a single H_2 gas bubble that forms in >4 ms. In these conditions, multiple smaller gas bubbles are observed at $\Delta t = 4$ ms. Crosses, aperiodic detachment of small gas bubbles. **m**, Phase diagram of different gas bubble evolution patterns at each condition. **n**, Transition point (potential/current) where the HER current starts periodic oscillation versus the anion partition coefficient. Solid black boxes and pink empty boxes indicate the onset potential of oscillation and the average current at that potential, respectively, revealing the strong correlation. In the case of 1 M H_2SO_4, the partition coefficient value of HSO_4^- is used.

Beyond a certain supersaturation level, multiple gas bubbles spontaneously nucleate on the electrode surface, resulting in complex interdependencies of various bubble behaviours during electrochemical water splitting[20–22]. Recent developments in micro- and nanoelectrode fabrication have made it possible to study the fundamental evolution of electrochemically generated gas bubbles by reducing this complexity and focusing on single gas bubble events. Nanoelectrodes (diameter, ≤100 nm) provide a unique platform to study the nucleation of a single nanobubble through a sudden current drop due to surface blockage[23,24]. Based on classical nucleation theory, heterogeneous nucleation was proposed for a H_2 nanobubble formed at a platinum nanoelectrode in H_2SO_4 (ref. 25). Moreover, single H_2 gas bubble detachment has been studied by using platinum microelectrodes in H_2SO_4, where the thermal Marangoni effect (mass transfer along an interface between two phases due to a surface tension gradient caused by a temperature gradient)[26,27] and electrostatic interaction between a gas bubble and the platinum electrode[28] were considered to be the main contributing forces determining gas bubble dynamics. Although these results provide basic

https://doi.org/10.1038/s41557-023-01294-y

physical models[29] on H_2 gas bubble nucleation and detachment during water electrolysis, the detailed effect of the electrolyte composition on gas bubble dynamics remains elusive.

Here we report that the type of anion in the acid electrolyte indeed greatly influences H_2 gas bubble dynamics during the HER. Using a platinum microelectrode as the platform electrode, detailed H_2 gas bubble dynamics are revealed through current oscillation measurements and high-speed imaging, while varying the type of anion. We find that the microbubble coalescence efficiency at a given potential follows a relation with the Hofmeister series of anions in the electrolyte. This difference in efficiency of microbubble coalescence results in very different H_2 gas bubble detachment behaviour: namely, periodic detachment of a single H_2 gas bubble in electrolytes such as H_2SO_4, in contrast to aperiodic detachment of small-sized H_2 gas bubbles, without the formation of a single large H_2 gas bubble, in electrolytes such as $HClO_4$. By carefully tuning the electrolyte composition, we further demonstrate that the solutal Marangoni force[30,31], that is, the force due to a surface tension gradient caused by a concentration gradient, plays the crucial role in determining the H_2 gas bubble detachment for the studied potential range. This important insight provides new avenues for tuning and controlling bubble coalescence and detachment during electrochemical gas bubble formation.

Results and discussion

Anion effects on HER current and H_2 gas bubble evolution

Figure 1a–d shows fluctuations and oscillations in HER currents during chronoamperometry measurements on the platinum microelectrode for various acidic electrolytes at 1 M concentration. The fluctuation and oscillation patterns depend on the type of anion in the acid electrolytes and on the applied potential; these patterns can be categorized as (1) periodic oscillation with a larger amplitude and (2) aperiodic fluctuation with a smaller amplitude. Parallel microscopic observation of the platinum microelectrode revealed that these HER current fluctuations reflect different patterns of the H_2 gas bubble evolution during the chronoamperometry measurement. For example, periodically oscillating HER currents were observed in H_2SO_4 and HCl at −0.16 V versus a reversible hydrogen electrode (V_{RHE}), and originated from the periodic formation and detachment of a single large H_2 gas bubble (Fig. 1e,f and Supplementary Videos 1 and 2). On the other hand, in HNO_3 and $HClO_4$ at −0.16 V_{RHE}, aperiodic fluctuations of HER currents were observed, which were associated with a multiple detachment of smaller gas bubbles of various sizes (Fig. 1g,h and Supplementary Videos 3 and 4). We consider possible specific anion effects on the HER kinetics on the platinum surface (nitrate reduction reaction and/or chloride adsorption) as minimal at the highly negative potential and large reductive current observed in our experiments[11,32,33].

The time synchronization between the electrochemical and microscopic measurements confirms the same periods for the HER current oscillation and the single H_2 gas bubble detachment. Once the single H_2 gas bubble has detached, a new single H_2 gas bubble is formed through the successive coalescence of small-sized microbubbles near the platinum surface (Supplementary Video 5). After the single H_2 gas bubble has formed, microbubbles near the platinum surface keep coalescing into the single H_2 gas bubble, resulting in the growth of the single H_2 gas bubble and a decrease in the HER current. When the single H_2 gas bubble has reached a certain size, it detaches, immediately followed by a sharp increase in HER current, which completes one cycle of the oscillation.

Although the single H_2 gas bubble evolution process in HCl is similar to that in H_2SO_4, the kinetics of single H_2 gas bubble formation is different due to the different microbubble coalescence behaviour. The inset images, showing an enlarged surface region taken at $\Delta t = 4$ ms after departure of the previous bubble, provide direct insight into microbubble coalescence in different electrolytes. A single H_2 gas bubble was already observed in H_2SO_4 at −0.16 V_{RHE}, whereas at the same potential in HCl, two or more smaller H_2 gas bubbles are seen to grow at this point in the cycle. Microbubble coalescence is even more inhibited in HNO_3 and $HClO_4$ electrolytes at −0.16 V_{RHE}, resulting in the random detachment of various smaller-sized gas bubbles without forming a single H_2 gas bubble (Fig. 1g,h). As the applied potential was decreased to −0.56 V_{RHE}, the periodic evolution of a single H_2 gas bubble can be observed regardless of the type of anion (Fig. 1i–l). The microbubble coalescence behaviours therefore depend on both anion type and applied potential (Supplementary Video 6 and Supplementary Figs. 1–4).

Figure 1m summarizes the different H_2 gas bubble evolution patterns during chronoamperometry measurement in a phase diagram. In particular, this figure clarifies how the H_2 gas bubble detachment mode changes with variation in the potential and/or anion type when the results are plotted in the order of H_2SO_4, HCl, HNO_3 and $HClO_4$: periodic detachment of a single large H_2 gas bubble (pink circles) is observed toward the upper left of the diagram, while non-periodic small-sized H_2 gas bubble detachment (light green crosses) is observed toward the lower right of the diagram. These two regimes are separated by an intermediate regime (light blue squares), where initial microbubble coalescence is disturbed during single bubble formation. A similar transition from the periodic detachment of a single H_2 gas bubble to the aperiodic detachment of small H_2 gas bubbles has been reported on a platinum microelectrode in H_2SO_4 after adding surfactant or ethylene glycol to the H_2SO_4 electrolyte[34]. The authors tried to analyse the correlation between gas bubble coalescence and surface tension, and

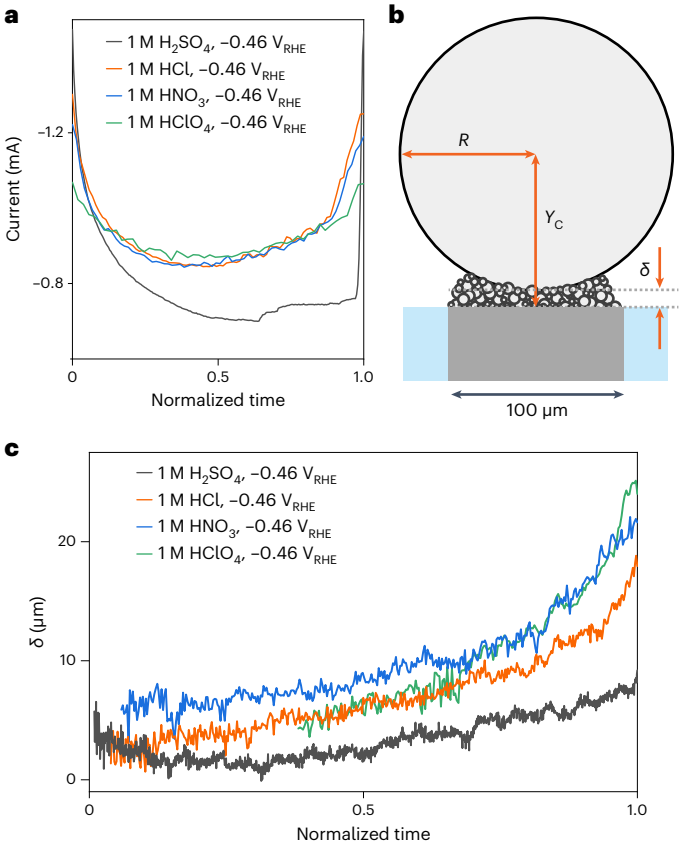

Fig. 2 | Anion effects during single H_2 gas bubble growth. a, Current transient curves during one cycle of oscillation. Time is normalized by the length of oscillation period in each electrolyte. **b**, Representation of single H_2 gas bubble growing with nearby microbubbles, defining R, Y_C and δ. **c**, Bubble carpet thickness (that is, $\delta = Y_C - R$, the distance between the platinum microelectrode surface and the base of a single H_2 gas bubble) during one oscillation.

https://doi.org/10.1038/s41557-023-01294-y

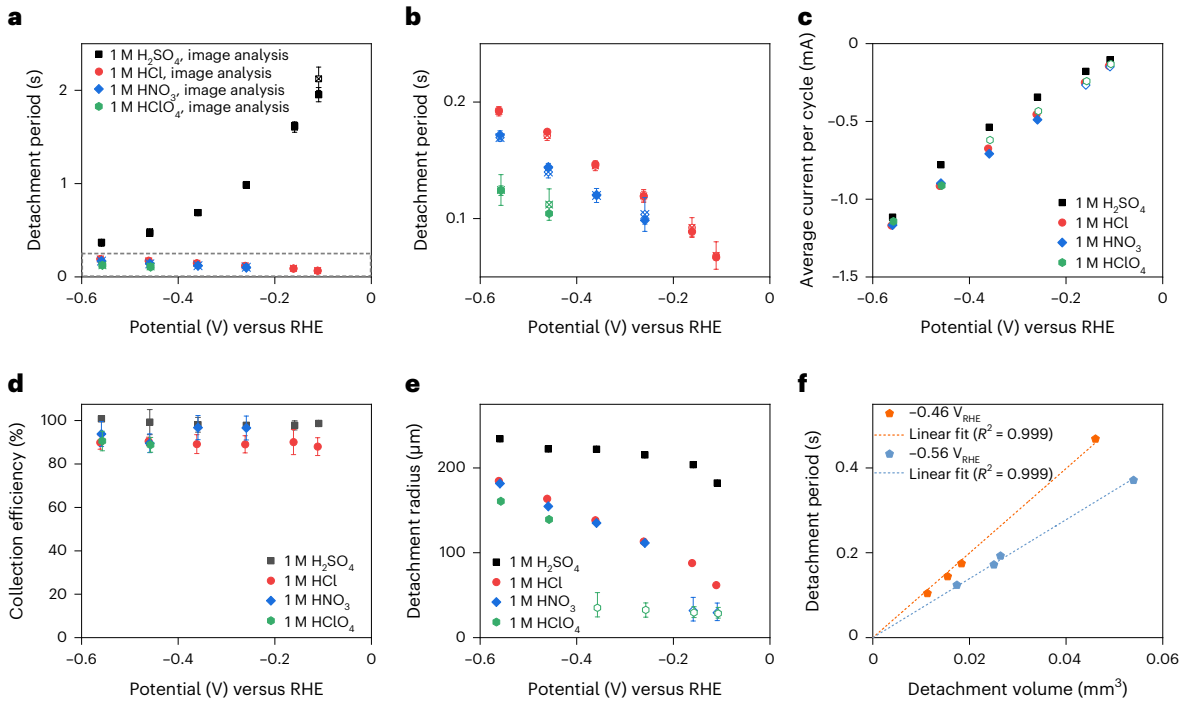

Fig. 3 | Anion effects on single H_2 gas bubble detachment. a, Detachment period as a function of the potential for four different electrolytes. **b**, Enlarged plot of the dashed grey box in **a**. Solid point data represent the average period with s.d. obtained from image analysis of eight different bubble cycles for each potential. Open point data indicate the average period with s.d. obtained from 50 HER current oscillations, except for H_2SO_4 where entire oscillations during 15 s of chronoamperometry were used due to the large period (Supplementary Fig. 9a provides specific sample sizes for each potential). Both image analysis and electrochemical oscillation analysis yield consistent period values within the error range. **c**–**e**, Change in average current (**c**), collection efficiency (**d**) and detachment radius (**e**) as a function of potential for each electrolyte. Collection efficiency is determined by the ratio of the amount of H_2 gas captured in a single gas bubble to the total amount of H_2 gas produced. Collection efficiency data are presented as average values with s.d. (sample size, 8). Solid dots and open dots in **c** and **e** correspond to data from the periodic formation/detachment of a single H_2 gas bubble and the detachment of small microbubbles, respectively. The open dots in **e** are presented as average values with the 10th and 90th percentiles of the distribution as boundaries (sample size, 4,950). **f**, Correlation between period and detachment volume.

suggested a critical surface tension value (~70 mN m^{-1}) as a descriptor for the transition point of the gas bubble detachment mode. However, the critical surface tension value cannot explain our observation because all the electrolytes we used have a surface tension >70 mN m^{-1} (Supplementary Table 1).

To further elucidate the transition between different H_2 gas bubble detachment modes, we check the onset potential and the corresponding current for the formation of a single H_2 gas bubble, which can be extracted from the onset potentials of HER current oscillation during chronoamperometry or linear sweep voltammetry (Fig. 1n and Supplementary Fig. 5). The overpotential/current for the onset of single H_2 gas bubble formation increases in the order H_2SO_4, HCl, HNO_3 and $HClO_4$, which coincides with the inverse order of the Hofmeister series of anions, a much-used classification for describing ion-specific effects[35]. Here we used the solute partitioning model of Pegram and Record to quantitatively describe the Hofmeister series[36]. Their model provides single ion partition coefficients based on the surface tension increment data, which represents the relative ion concentration at the air/electrolyte interface compared to the bulk electrolyte concentration. Considering that a single H_2 gas bubble is formed by microbubble coalescence, the observed trend implies a correlation between the coalescence of electrochemically generated microbubbles and the propensity of ions at the bubble/electrolyte interface.

In general, the gas bubble coalescence can be analysed by considering the gas bubble collision frequency and the coalescence efficiency, which is the likelihood of collisions resulting in coalescence[37,38]. It is known that some specific ion combinations in aqueous solution can hugely reduce the coalescence efficiency of gas bubbles when the ion concentration is above a certain critical value[39]. According to the empirical α/β categorization by Craig[39], one would expect severe coalescence inhibition of gas bubbles for $HClO_4$ when the concentration is higher than 70 mM (ref. 40). In contrast, no substantial coalescence inhibition was observed in H_2SO_4, HCl and HNO_3 below 500 mM (ref. 40). A more gradual change in the gas bubble coalescence inhibition was reported with the addition of bulky tetraalkylammonium cations[41]. Although a number of explanations have been proposed concerning the origin of coalescence inhibition, there is still no definitive agreement on explaining the underlying mechanism of coalescence inhibition and the specific ion effects[42,43].

Based on the above gas bubble coalescence model, we can consider the contribution of collision frequency and coalescence efficiency to the observed anion effect on microbubble coalescence at a fixed potential. The collision frequency of microbubbles within the electrolyte depends on their number density. At a given potential, the collision frequency would be similar for different electrolytes, considering that (1) the same surface structure of platinum electrode applies for all measurements, (2) similar current levels are observed (thus, similar H_2 supersaturation) and (3) H_2 nanobubble nucleation on a platinum nanoelectrode has observed to be anion independent[44]. Therefore, we conclude that the observed anion-dependent coalescence behaviour originates from the different coalescence efficiencies of electrochemically generated microbubbles, following the anion propensity at the bubble/electrolyte interface: the microbubble coalescence efficiency follows the Hofmeister series of anions in the electrolyte. In the case of the mode transition observed when varying the applied potential in HNO_3 or $HClO_4$, both collision frequency and coalescence efficiency can

contribute to the transition to periodic single H_2 gas bubble detachment above a certain critical overpotential (see Supplementary Note 1 for further discussion).

Anion effects on single H_2 gas bubble growth

According to Fig. 1m, periodic single H_2 gas bubble evolution can be observed from all electrolytes when a large enough overpotential is applied. Interestingly, the HER current transients during the growth of a single H_2 gas bubble are also anion dependent (Supplementary Fig. 6). Figure 2a shows the HER current transient during one cycle of oscillation at −0.46 V_{RHE}, normalized by the period of oscillation. In H_2SO_4, after the initial HER current decreased, the current stays relatively constant, until its sudden increase at the detachment moment, leading to an asymmetric shape about the minimum current. On the other hand, in HCl, HNO_3 and $HClO_4$ electrolytes, the HER current first decreases and then keeps slowly increasing, thus leading to much more symmetric shape about the minimum current. Furthermore, the magnitude of the minimum current in these electrolytes is larger than the value in H_2SO_4. Note that the smaller magnitude of the minimum current in H_2SO_4 cannot be explained by differences in bulk electrical conductivity between electrolytes (Supplementary Table 1). We speculate that this lower current might be attributed to differences in the exposed surface area and the local ion distribution (and thus, changes in local conductivity)[45] caused by the gas bubbles.

To gain more insight into the anion effects on the HER current, we analysed the dynamics and geometry of H_2 gas bubbles during one cycle of oscillation. The growth patterns are similar regardless of the electrolyte and applied potential (Supplementary Fig. 7). In all cases, the radius evolution approximately follows a power law in time $R \propto t^x$, with the exponent x close to 1/3, consistent with reaction-limited growth of the H_2 bubble[46,47]. Note that the growth of the single H_2 gas bubble occurs via coalescence with a microbubble cluster, the so-called bubble carpet[28], located underneath the single bubble (see sketch in Fig. 2b and Supplementary Video 5). While the precise analysis of individual microbubbles is challenging due to their overlap in the projected image, the thickness of the bubble carpet (δ) can be indirectly deduced from the position (Y_C) and radius (R) of a single H_2 gas bubble ($\delta = Y_C - R$, as shown in Fig. 2b).

In contrast to the similar growth rate law of a single H_2 gas bubble for all electrolytes, δ in H_2SO_4 has distinguishable features compared to the other three electrolytes (Fig. 2c and Supplementary Fig. 8). In H_2SO_4, δ first decreases during the initial growth stage, followed by a slight increase up to 8 µm. By contrast, in HCl, HNO_3 and $HClO_4$, δ increases monotonically during the growth of a single H_2 gas bubble, reaching values of 19–25 µm. Thus, the observed difference in HER current transient between H_2SO_4 and other electrolytes is probably associated with the difference in δ. In particular, the current is seen to recover simultaneously with the increase in δ in the other electrolytes (HCl, HNO_3 and $HClO_4$), whereas the minimal change of δ in H_2SO_4 is consistent with the plateau shape of the HER current for this case. This correlation can be rationalized noting that presumably less surface is blocked as the bubble carpet expands, resulting in the increase of the HER current.

Anion effects on single H_2 gas bubble detachment

The period of a single H_2 gas bubble evolution also strongly depends on the type of anion in the electrolyte (Fig. 3 and Supplementary Fig. 9). Across the entire potential region investigated, the detachment periods always follow the sequence: $H_2SO_4 \gg HCl > HNO_3 > HClO_4$ (Fig. 3a,b). In particular, the detachment of a single H_2 gas bubble in H_2SO_4 was much slower than in the other three electrolytes. For example, the period in H_2SO_4 at −0.16 V_{RHE} is 1.619 s, which is more than an order of magnitude larger than the period of 0.092 s in HCl at −0.16 V_{RHE}. Furthermore, the potential-dependent trend of the detachment period in H_2SO_4 is opposite to the trends in the other three electrolytes. As the applied overpotential decreases, the detachment of a single H_2 gas bubble becomes slower in H_2SO_4, whereas the detachment becomes faster in the other three electrolytes (Fig. 3a). The same anion trend was observed when plotted versus the average current instead of the applied potential (Supplementary Fig. 10).

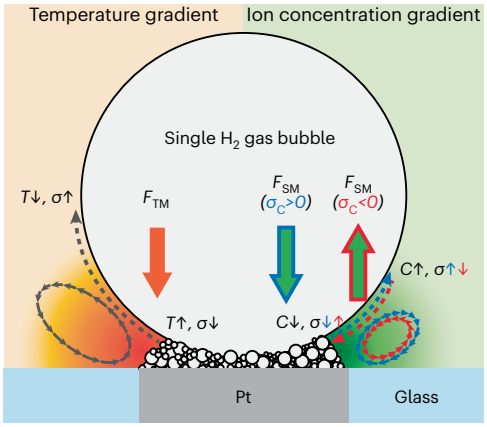

Fig. 4 | Schematic illustration of the thermal and solutal Marangoni effects on H_2 gas bubble evolution. Left: orange colour gradient depicts the temperature field during the HER. Thermal Marangoni (TM) flow induced by temperature gradient points away from the platinum surface region (black arrows). Right: green colour gradient depicts the ion concentration field during the HER. Solutal Marangoni (SM) flow induced by concentration gradient with positive surface tension increment ($\partial\sigma/\partial C \equiv \sigma_C > 0$) away from the platinum surface region (blue arrows). Solutal Marangoni flow induced by concentration gradient with negative surface tension increment ($\sigma_C < 0$) towards the platinum surface region (red arrows). Note that the solutal boundary layer is much thinner by a factor of $\sqrt{\mathrm{Le}}$ than the thermal one because the mass diffusivity is smaller than the thermal diffusivity (where $\mathrm{Le} = \kappa/D$ is the Lewis number, that is, the ratio between thermal diffusivity and mass diffusivity; typically, $\mathrm{Le} \approx 100$)[31].

To further elucidate the origin of the different trends as a function of applied potential, we note that the period (τ), the detachment radius (R_D) and the average current ($\bar{I}$) are related via (see the experimental section for derivation)

$$\tau = \frac{-8\pi F P_0 R_D^3}{3RT\bar{I} \times (\mathrm{CE}/100)}, \quad (1)$$

where F, P_0, R, T and CE are the Faraday constant, the atmospheric pressure, the gas constant, the temperature and the collection efficiency of a single H_2 gas bubble, respectively. Figure 3c shows averaged currents per cycle for different electrolytes. As the overpotential increases, the magnitude of the averaged current in all electrolytes increases as well. Although the magnitude of average current in H_2SO_4 was slightly smaller than that of the other three electrolytes, this difference is not enough to explain the large difference in the detachment periods between H_2SO_4 and other electrolytes. The collection efficiency of a single H_2 gas bubble is >90% under most conditions and approaches 100%, especially in H_2SO_4 (Fig. 3d). This indicates that essentially all of the H_2 gas produced at the platinum microelectrode is captured by the single bubble, which is consistent with earlier findings[48]. In contrast to the averaged current and collection efficiency, large differences were observed in the detachment radius between H_2SO_4 and other electrolytes, which showed the same tendency as the observed electrolyte sequence for τ (Fig. 3e). Considering that τ is proportional to the cube of the detachment radius (that is, the detachment volume), the difference in radius can explain an order of magnitude difference of τ between H_2SO_4 and HCl. Correlation curves further confirm that the difference in detachment radius is the main origin of the observed anion effect on the period (Fig. 3f and Supplementary Fig. 11).

https://doi.org/10.1038/s41557-023-01294-y

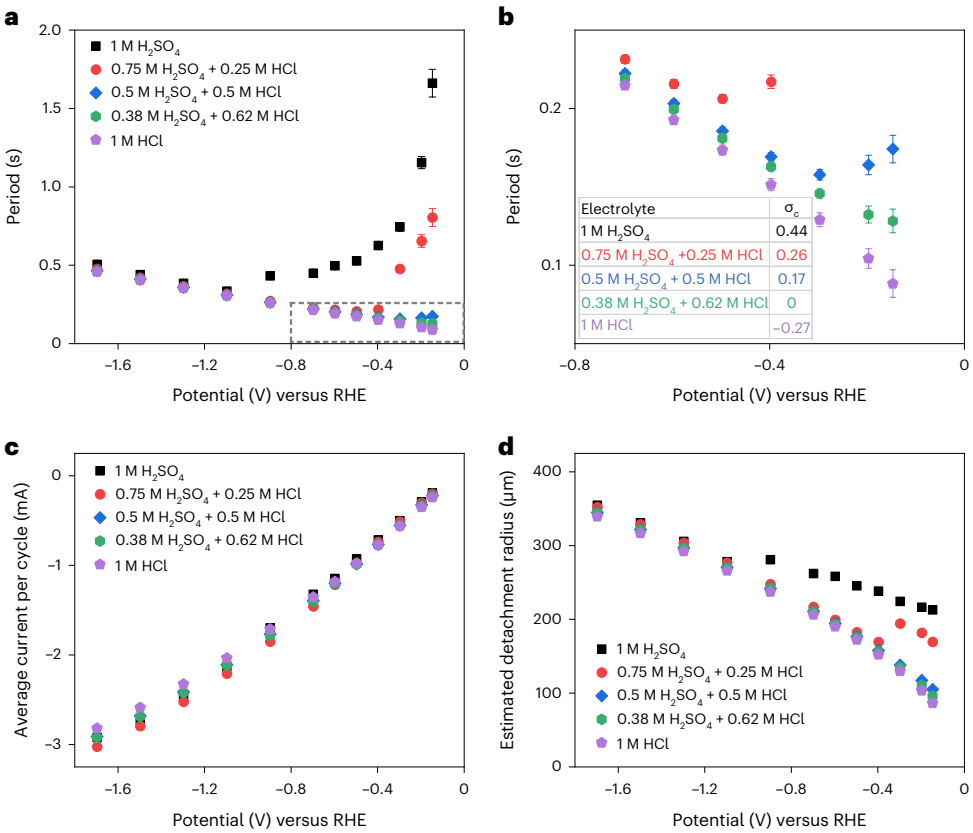

Fig. 5 | HER current oscillations in mixed electrolytes of H_2SO_4 and HCl. **a**, Period trend as a function of potential for different electrolytes. **b**, Enlarged plot of the dashed grey box in **a**. Inset: surface tension increment values for each electrolyte. Period data are presented as average values with error bars representing the s.d. For statistical analysis, 50 HER current oscillations were used when the period was <0.3 s, while the entire HER current oscillations during 15 s of chronoamperometry were used when the period was >0.3 s (specific sample sizes under these conditions can be found in Supplementary Fig. 14). **c**,**d**, Average current per oscillation cycle (**c**) and estimated detachment radius (**d**) for different electrolytes. The detachment radius is estimated assuming 100% collection efficiency.

It is noteworthy that the bubble size distributions in the case of small microbubble detachment (see error bars of open symbols, representing 10th and 90th percentiles, in Fig. 3e and Supplementary Fig. 12) also feature consistent trends, that is, larger bubbles are formed in HNO_3 compared to $HClO_4$ and as the current increases with increasing overpotential. The maximum bubble radii encountered in the non-periodic small microbubble detachment cases are about 65 μm. It appears that microbubbles need to coalesce rapidly enough in the vicinity of the electrode to reach sizes somewhat larger than this to be retained (for example, by electrostatic and Marangoni forces) for continued growth. This implies that in the context of electrochemically generated microbubbles, the fact that the coalescence efficiency changes more gradually compared to Craig's α/β categorization[39] is of considerable relevance because this renders bubble dynamics strongly and nonlinearly dependent on the operating conditions.

The different detachment radius for each anion indicates a different force equilibrium at the moment of detachment. Recently, a detailed force balance of a single H_2 bubble on platinum microelectrode in H_2SO_4 was proposed by the Eckert group[49]. They considered a force equilibrium among the buoyancy force, the electrical force, the hydrodynamic force and the thermal Marangoni force. Notably, the temperature gradient from local ohmic heating near the platinum surface can induce a Marangoni flow, for which the resulting force on the bubble is towards the electrode[27]. The buoyancy force of an electrochemically generated gas bubble also requires the consideration of local density changes due to the ion concentration gradient development, which was confirmed through the natural convection induced at microelectrodes[50].

However, the anion dependence of the detachment radius cannot be explained by the solutal buoyancy force, the electrical force or the thermal Marangoni force presented above. The decrease in ion concentration near the platinum surface leads to a reduced local density of the electrolyte, which in turn slightly enhances the effective buoyancy force on the gas bubble. However, while the buoyancy force is expected to be further enhanced with increasing current, its dependence on anion type is negligible due to the small differences in bulk density observed among the different electrolytes (Supplementary Table 1). At a fixed potential, the magnitude of the electrical force is determined by the surface charge of a single H_2 gas bubble[51]. Because of the similar pH values of the four electrolytes (Supplementary Table 1), the magnitude of the electrical force is also expected to be similar for all electrolytes. The thermal Marangoni force is determined by the temperature gradient along the gas bubble/electrolyte interface, which, given that other factors such as geometry and conductivity are similar, can be assumed to be proportional to the ohmic heating ($\sim I^2$) near the platinum surface. Once a single H_2 gas bubble is formed, the magnitude of the HER current is smaller in H_2SO_4 than in the other electrolytes (Fig. 2a and Supplementary Fig. 13). Therefore, a single H_2 gas bubble in H_2SO_4 would experience a smaller downward-directed thermally driven Marangoni force compared with other electrolytes. This should lead to earlier detachment in the H_2SO_4 case, which is the opposite of what is observed experimentally.

This inconsistency made us consider another possibility, namely the solutal Marangoni effect[30,31], because the ion concentration gradient is also able to alter the surface tension. In fact, the solutal Marangoni force in a binary liquid is in general stronger than the thermal one, although the range is smaller because the thickness of the solutal boundary layer is smaller than that of the thermal one due to the much smaller mass diffusivity as compared to the thermal diffusivity[52]. Notably, the surface tension increases with increasing concentration of H_2SO_4 (surface tension increment σ_C, $\sigma_C \equiv \partial\sigma/\partial C$, $\sigma_C > 0$)[42], whereas surface tension is decreasing with increasing concentration of HCl, HNO_3 and $HClO_4$ ($\sigma_C < 0$)[42] (Supplementary Table 1). As illustrated in Fig. 4, the region near the platinum surface has a lower ion concentration than the bulk region due to the fast proton consumption which leads to a corresponding anion concentration gradient along the bubble/electrolyte interface to satisfy electroneutrality. In the case of H_2SO_4, a lowered ion concentration near the platinum surface region lowers the local surface tension. Consequently, the solutal Marangoni flow along the bubble surface steers away from the platinum surface, and therefore the solutal Marangoni force would act towards the electrode. Although a similar ion concentration gradient is developed in HCl, HNO_3 and $HClO_4$, the surface tension gradient is reversed due to the negative σ_C. Therefore, the expected direction of the solutal Marangoni force is then away from the electrode. This reversed solutal Marangoni force vector for H_2SO_4 compared to HCl, HNO_3 and $HClO_4$ is perfectly consistent with the observed anion sequence for the periodic detachment radius of a single H_2 gas bubble ($H_2SO_4 \gg HCl > HNO_3 > HClO_4$). In addition, at approximately 0.3 μN, the buoyancy force difference implied by the different detachment radii is consistent in magnitude with the values of order 1 μN typically reported for Marangoni-induced forces in related studies[27,49,53]. Therefore, we hypothesize that it is the solutal Marangoni force induced by the ion concentration gradient which is the critical factor in determining the single H_2 gas bubble detachment radius under our measurement conditions. It is worth mentioning that the different directions of the solutal Marangoni force acting on the single H_2 gas bubble might also explain the previously discussed differences in the evolution of the microbubble carpet thickness (δ in Fig. 2c).

To further support this hypothesis, we prepared electrolytes of various σ_C values and analysed the period through chronoamperometry measurements. The σ_C was controlled by mixing 1 M H_2SO_4 and 1 M HCl in various ratios. These electrolytes feature the highest coalescence efficiencies among all electrolytes we used, which ensures that the single bubble regime extends to the very small overpotential region. Since the solutal Marangoni force induced by the ion concentration gradient is proportional to σ_C, the expectation under the above hypothesis is that σ_C and τ would follow a consistent trend. As Fig. 5a,b and Supplementary Figs. 14 and 15 confirm, this is indeed what happens for all conditions we investigated: values of τ are found to be larger the higher the σ_C of the electrolyte. However, this electrolyte dependence reduces for very large overpotential conditions. Additionally, periods are seen to decrease when the applied overpotential is reduced when there is little electrolyte dependence, whereas the opposite is true in potential regions exhibiting strong electrolyte dependence of τ. These differences clearly point towards competing mechanisms dominating in the respective regions.

As discussed above, a strong electrolyte-dependent τ in the small overpotential regions can be rationalized by the electrolyte-dependent solutal Marangoni force. Instead, electrolyte-independent thermal driving of the Marangoni convection might be dominant in very large overpotential regions, where the τ trend becomes independent of the electrolyte identity. This notion is strongly supported by previous investigations that identified thermal driving as the relevant mechanism at very large overpotentials[27,53]. Moreover, a change in the dominant Marangoni effect as a function of the overpotential, and consequently of the current, seems reasonable, considering that the ion concentration gradient scales with $\bar{I}$ while the thermal driving approximately scales with $\bar{I}^2$. Furthermore, the direction of the thermal Marangoni force (Fig. 4) and its magnitude trend[27,49,53] explain the decreasing trends for the detachment radius and the period (Fig. 5d,a, respectively) when the overpotential is reduced (see Supplementary Note 2 for more discussion).

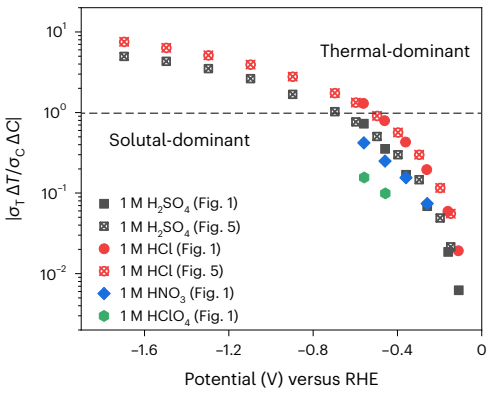

Fig. 6 | Surface tension change ratio due to the temperature and ion concentration ($\sigma_T = \partial\sigma/\partial T$ and $\sigma_C = \partial\sigma/\partial C$) as function of the applied potential. The dominant origins of surface tension gradient are the temperature gradient at the area above the dashed line and the ion concentration gradient at the area below the dashed line.

To approximate this competition quantitatively, we compare estimates for the surface tension change from temperature and concentration gradients (see the experimental section for details on the calculation). The plot of the surface tension change ratio between temperature ($\sigma_T \Delta T$) and concentration ($\sigma_C \Delta C$) variation (Fig. 6) supports our conclusion that the solutal Marangoni effect is dominant in small overpotential regions. Notably, the potential at which the ratio is 1 can be tentatively used as an expected boundary for the region where the solutal Marangoni effect is dominant. In 1 M H_2SO_4, the boundary potential is −0.7 V_{RHE} (−1.3 mA) corresponding to the geometric current density (J) of −17 A cm^{-2}. This implies that the solutal Marangoni effect must be taken into account for H_2 gas bubble manipulation under most practical current density conditions[3,5].

Conclusions

In this work, we have presented the effect of anions in acidic electrolytes on H_2 gas bubble dynamics during the HER on a platinum microelectrode. The H_2 gas bubble detachment mode is sensitively dependent on the type of anion due to the different microbubble coalescence efficiency, which follows the Hofmeister series of anions in the electrolyte. We conclude that at practically relevant current densities, the solutal Marangoni force, induced by ion concentration gradients, determines bubble detachment as opposed to the thermal Marangoni force which becomes relevant at very large overpotentials (with a current density of $|J| > 17$ A cm^{-2}). Because the surface tension increment varies for the different electrolytes, the resulting solutal Marangoni forces acting on the single H_2 gas bubble also change. Ultimately, this leads to different H_2 gas bubble detachment radii and periods according to the type of anion in the electrolyte. The results of this work unravel important physicochemical aspects of electrochemically generated H_2 gas bubbles. These findings lead to an in-depth understanding of H_2 gas bubble dynamics at the electrode/electrolyte/gas bubble interface, which provides valuable insights into gas bubble manipulation for the optimization of gas-evolving electrochemical systems.

Online content

Any methods, additional references, Nature Portfolio reporting summaries, source data, extended data, supplementary information, acknowledgements, peer review information; details of author contributions and competing interests; and statements of data and code availability are available at https://doi.org/10.1038/s41557-023-01294-y.

References

1. Turner, J. A. Sustainable hydrogen production. *Science* **305**, 972–974 (2004).
2. Ardo, S. et al. Pathways to electrochemical solar-hydrogen technologies. *Energy Environ. Sci.* **11**, 2768–2783 (2018).
3. Buttler, A. & Spliethoff, H. Current status of water electrolysis for energy storage, grid balancing and sector coupling via power-to-gas and power-to-liquids: a review. *Renew. Sustain. Energy Rev.* **82**, 2440–2454 (2018).
4. Shih, A. J. et al. Water electrolysis. *Nat. Rev. Methods Primers* **2**, 84 (2022).
5. Chatenet, M. et al. Water electrolysis: from textbook knowledge to the latest scientific strategies and industrial developments. *Chem. Soc. Rev.* **51**, 4583–4762 (2022).
6. Seh, Z. W. et al. Combining theory and experiment in electrocatalysis: insights into materials design. *Science* **355**, eaad4998 (2017).
7. Dubouis, N. & Grimaud, A. The hydrogen evolution reaction: from material to interfacial descriptors. *Chem. Sci.* **10**, 9165–9181 (2019).
8. Ledezma-Yanez, I. et al. Interfacial water reorganization as a pH-dependent descriptor of the hydrogen evolution rate on platinum electrodes. *Nat. Energy* **2**, 1–7 (2017).
9. Li, P. et al. Hydrogen bond network connectivity in the electric double layer dominates the kinetic pH effect in hydrogen electrocatalysis on Pt. *Nat. Catal.* **5**, 900–911 (2022).
10. Diaz-Morales, O., Ferrus-Suspedra, D. & Koper, M. T. M. The importance of nickel oxyhydroxide deprotonation on its activity towards electrochemical water oxidation. *Chem. Sci.* **7**, 2639–2645 (2016).
11. Kamat, G. A. et al. Acid anion electrolyte effects on platinum for oxygen and hydrogen electrocatalysis. *Commun. Chem.* **5**, 20 (2022).
12. Garcia, A. C., Touzalin, T., Nieuwland, C., Perini, N. & Koper, M. T. M. Enhancement of oxygen evolution activity of nickel oxyhydroxide by electrolyte alkali cations. *Angew. Chem. Int. Ed.* **58**, 12999–13003 (2019).
13. Dukovic, J. & Tobias, C. W. The influence of attached bubbles on potential drop and current distribution at gas-evolving electrodes. *J. Electrochem. Soc.* **134**, 331–343 (1987).
14. Gabrielli, C., Huet, F. & Nogueira, R. P. Fluctuations of concentration overpotential generated at gas-evolving electrodes. *Electrochim. Acta* **50**, 3726–3736 (2005).
15. Vogt, H. & Balzer, R. J. The bubble coverage of gas-evolving electrodes in stagnant electrolytes. *Electrochim. Acta* **50**, 2073–2079 (2005).
16. Vogt, H. The voidage problem in gas-electrolyte dispersions. *J. Appl. Electrochem.* **17**, 419–426 (1987).
17. Fouad, M. G. & Sedahmed, G. H. Mass transfer at horizontal gas-evolving electrodes. *Electrochim. Acta* **18**, 55–58 (1973).
18. Xu, W., Lu, Z., Sun, X., Jiang, L. & Duan, X. Superwetting electrodes for gas-involving electrocatalysis. *Acc. Chem. Res.* **51**, 1590–1598 (2018).
19. Angulo, A., van der Linde, P., Gardeniers, H., Modestino, M. & Fernández Rivas, D. Influence of bubbles on the energy conversion efficiency of electrochemical reactors. *Joule* **4**, 555–579 (2020).
20. Zhao, X., Ren, H. & Luo, L. Gas bubbles in electrochemical gas evolution reactions. *Langmuir* **35**, 5392–5408 (2019).
21. Yang, S. et al. Electrolytically generated nanobubbles on highly orientated pyrolytic graphite surfaces. *Langmuir* **25**, 1466–1474 (2009).
22. van der Linde, P. et al. Electrolysis-driven and pressure-controlled diffusive growth of successive bubbles on microstructured surfaces. *Langmuir* **33**, 12873–12886 (2017).
23. Luo, L. & White, H. S. Electrogeneration of single nanobubbles at sub-50-nm-radius platinum nanodisk electrodes. *Langmuir* **29**, 11169–11175 (2013).
24. Soto, A. M. et al. The nucleation rate of single O_2 nanobubbles at Pt nanoelectrodes. *Langmuir* **34**, 7309–7318 (2018).
25. German, S. R., Edwards, M. A., Ren, H. & White, H. S. Critical nuclei size, rate, and activation energy of H_2 gas nucleation. *J. Am. Chem. Soc.* **140**, 4047–4053 (2018).
26. Yang, X., Baczyzmalski, D., Cierpka, C., Mutschke, G. & Eckert, K. Marangoni convection at electrogenerated hydrogen bubbles. *Phys. Chem. Chem. Phys.* **20**, 11542–11548 (2018).
27. Massing, J. et al. Thermocapillary convection during hydrogen evolution at microelectrodes. *Electrochim. Acta* **297**, 929–940 (2019).
28. Bashkatov, A., Hossain, S. S., Yang, X., Mutschke, G. & Eckert, K. Oscillating hydrogen bubbles at Pt microelectrodes. *Phys. Rev. Lett.* **123**, 214503 (2019).
29. Lohse, D. & Zhang, X. Surface nanobubbles and nanodroplets. *Rev. Mod. Phys.* **87**, 981 (2015).
30. Scriven, L. E. & Sternling, C. V. The Marangoni effects. *Nature* **187**, 186–188 (1960).
31. Lohse, D. & Zhang, X. Physicochemical hydrodynamics of droplets out of equilibrium. *Nat. Rev. Phys.* **2**, 426–443 (2020).
32. Lamy-Pitara, E., El Mouahid, S. & Barbier, J. Effect of anions on catalytic and electrocatalytic hydrogenations and on the electrocatalytic oxidation and evolution of hydrogen on platinum. *Electrochim. Acta* **45**, 4299–4308 (2000).
33. de Groot, M. T. & Koper, M. T. M. The influence of nitrate concentration and acidity on the electrocatalytic reduction of nitrate on platinum. *J. Electroanal. Chem.* **562**, 81–94 (2004).
34. Fernandez, D., Maurer, P., Martine, M., Coey, J. M. D. & Möbius, M. E. Bubble formation at a gas-evolving microelectrode. *Langmuir* **30**, 13065–13074 (2014).
35. Zhang, Y. & Cremer, P. S. Interactions between macromolecules and ions: the Hofmeister series. *Curr. Opin. Chem. Biol.* **10**, 658–663 (2006).
36. Pegram, L. M. & Record, M. T. Hofmeister salt effects on surface tension arise from partitioning of anions and cations between bulk water and the air–water interface. *J. Phys. Chem. B* **111**, 5411–5417 (2007).
37. Prince, M. J. & Blanch, H. W. Bubble coalescence and break-up in air-sparged bubble columns. *AlChE J.* **36**, 1485–1499 (1990).
38. Liao, Y. & Lucas, D. A literature review on mechanisms and models for the coalescence process of fluid particles. *Chem. Eng. Sci.* **65**, 2851–2864 (2010).
39. Craig, V. S. & Henry, C. L. *Specific Ion Effects* (World Scientific, 2010).
40. Craig, V. S. J., Ninham, B. W. & Pashley, R. M. The effect of electrolytes on bubble coalescence in water. *J. Phys. Chem.* **97**, 10192–10197 (1993).
41. Monzon, L. M. A., Gillen, A. J., Mobius, M. E. & Coey, J. M. D. Effect of tetraalkylammonium cations on gas coalescence at a hydrogen-evolving microelectrode. *Langmuir* **31**, 5738–5747 (2015).
42. Weissenborn, P. K. & Pugh, R. J. Surface tension of aqueous solutions of electrolytes: relationship with ion hydration, oxygen solubility, and bubble coalescence. *J. Colloid Interface Sci.* **184**, 550–563 (1996).
43. Firouzi, M., Howes, T. & Nguyen, A. V. A quantitative review of the transition salt concentration for inhibiting bubble coalescence. *Adv. Colloid Interface Sci.* **222**, 305–318 (2015).
44. Chen, Q., Luo, L., Faraji, H., Feldberg, S. W. & White, H. S. Electrochemical measurements of single H_2 nanobubble nucleation and stability at Pt nanoelectrodes. *J. Phys. Chem. Lett.* **5**, 3539–3544 (2014).

45. Newton, M. R. et al. Anisotropic diffusion in face-centered cubic opals. *Nano Lett.* **4**, 875–880 (2004).
46. Brandon, N. P. & Kelsall, G. H. Growth kinetics of bubbles electrogenerated at microelectrodes. *J. Appl. Electrochem.* **15**, 475–484 (1985).
47. Wang, Y. et al. Vapor and gas-bubble growth dynamics around laser-irradiated, water-immersed plasmonic nanoparticles. *ACS Nano* **11**, 2045–2051 (2017).
48. Yang, X., Karnbach, F., Uhlemann, M., Odenbach, S. & Eckert, K. Dynamics of single hydrogen bubbles at a platinum microelectrode. *Langmuir* **31**, 8184–8193 (2015).
49. Hossain, S. S., Bashkatov, A., Yang, X., Mutschke, G. & Eckert, K. Force balance of hydrogen bubbles growing and oscillating on a microelectrode. *Phys. Rev. E* **106**, 035105 (2022).
50. Gao, X., Lee, J. & White, H. S. Natural convection at microelectrodes. *Anal. Chem.* **67**, 1541–1545 (1995).
51. Brandon, N. P., Kelsall, G. H., Levine, S. & Smith, A. L. Interfacial electrical properties of electrogenerated bubbles. *J. Appl. Electrochem.* **15**, 485–493 (1985).
52. Zeng, B. et al. Periodic bouncing of a plasmonic bubble in a binary liquid by competing solutal and thermal Marangoni forces. *Proc. Natl Acad. Sci. USA* **118**, e2103215118 (2021).
53. Meulenbroek, A. M., Vreman, A. W. & Deen, N. G. Competing Marangoni effects form a stagnant cap on the interface of a hydrogen bubble attached to a microelectrode. *Electrochim. Acta* **385**, 138298 (2021).

Methods

Chemicals

The electrolytes were prepared from H_2SO_4 (96%, Suprapur, Merck), HCl (30%, Suprapur, Merck), HNO_3 (65%, Suprapur, Merck), $HClO_4$ (60%, EMSURE, Merck) and Milli-Q water (≥18.2 MΩcm).

Microelectrode preparation

The platinum microelectrode was prepared by sealing platinum wire (100 µm, 99.99%, Goodfellow) in a soda-lime glass capillary (1.4 mm outside diameter, 1.12 mm inside diameter, Hilgenberg) with a butane torch. The prepared polycrystalline platinum microelectrode was first polished with diamond polishing suspensions of decreasing particle size (3, 1, 0.25, 0.05 µm, Buehler) on micropolishing cloths and then polished with sandpaper (P2000, Starcke). Between each polishing process, the electrode was sonicated in Milli-Q water to remove any residual impurities. Finally, the platinum surface was additionally cleaned by oxidation–reduction cycling between 0.03 and 1.35 V_{RHE} (30 times at 1 V s^{-1}) in N_2-purged 1 M H_2SO_4. The cleanliness of the prepared platinum surface was verified by cyclic voltammetry (Supplementary Fig. 16).

Electrochemical characterization

The experiments were performed in a one-compartment and three-electrode custom-made PEEK electrochemical cell which has a transparent glass window at the side (Supplementary Fig. 17). A platinum microelectrode was placed facing upwards to study the freely detachable H_2 gas bubble. A platinum wire (99.9%, MaTeck) and leakless Ag/AgCl (ET072-1, eDAQ) were used as counterelectrode and reference electrode, respectively. The electrochemical cell and glass window were stored in permanganate solution (0.5 M H_2SO_4 and 1 g l^{-1} $KMnO_4$). Before the experiment, any residual $KMnO_4$ and MnO_2 were removed from the electrochemical cell and glass window by dipping them in a diluted piranha solution. Then, the electrochemical cell and glass window were cleaned by boiling them five times in Milli-Q water. By using a Biologic (VSP-300) potentiostat, chronoamperometry measurements were carried out for 15 s at desired potentials where the HER takes place. Between each measurement, N_2 purging was performed for 20 min to remove H_2 gas in the electrolyte. All data presented in Figs. 1–3 were obtained using the same platinum microelectrode and were measured in the order of 1 M H_2SO_4, 1 M $HClO_4$, 1 M HNO_3 and 1 M HCl. The electrochemical cell and platinum microelectrode were thoroughly rinsed with Milli-Q water whenever the electrolyte was changed. Although the exact values (current and period) slightly depend on the electrode, the same electrolyte-dependent trends in H_2 gas bubble behaviour were confirmed by separate experiments with different platinum microelectrodes. Electrochemical data were plotted without ohmic resistance correction. In the case of periodically oscillating HER current, the period of each oscillation was determined by the peak positions from the chronoamperometry curve.

Optical characterization and image processing

A high-speed camera (Photron Fastcam Nova S16; frame rate, 3,000 f.p.s.) equipped with a magnification objective (12× Navitar) was used to observe the bubble dynamics during chronoamperometry at a resolution of 1.3 µm per pixel. Illumination was provided by three light sources (Schott KL2500), which were placed in front of the cell. Optical and chronoamperometric measurements were synchronized using a trigger signal. Image processing to extract the bubble edge and to obtain the bubble radius and its position was performed in MATLAB using a calibration based on the wire thickness. A minimum of eight bubbles were analysed for each case (except for those with the longest periods where the numbers were limited by the total recording time of 7.3 s) to obtain the radius and error bars indicating the variation in this set.

Relation between bubble detachment period, radius and average current

The amount of H_2 gas in a detached single gas bubble ($n_{H2,single\ gas\ bubble}$) is given by the ideal gas equation:

$$n_{H2,single\ gas\ bubble} = \frac{PV}{RT} \cong \frac{4\pi P_0 R_D^3}{3RT}$$

$$P = P_0 + \rho gh + 2\sigma/R_D \cong P_0$$

where R, T, P_0, R_D, ρgh and $2\sigma/R_D$ are the gas constant, the temperature, the atmospheric pressure, the detachment radius of a single gas bubble, the hydrostatic pressure and the Laplace pressure, respectively. Here we can safely neglect contributions from the hydrostatic (~$0.004P_0$) and the Laplace pressure (~$0.032P_0$), considering the electrolyte height (~4 cm) and the gas bubble size (~100 µm).

At the same time, the H_2 gas produced during its growth period ($n_{H2,produced}$) can be described by the application of Faraday's law:

$$n_{H2,produced} = \frac{\tau \times \bar{I}}{-2F},$$

where τ, $\bar{I}$ and F are the period, average current per cycle and the Faraday constant, respectively. The $n_{H2,single\ gas\ bubble}$ and $n_{H2,produced}$ are related by the collection efficiency (CE) of a single gas bubble ($CE\,(\%) = n_{H2,large\ gas\ bubble}/n_{H2,produced}$). This leads to the following equation:

$$\tau = \frac{-8\pi F P_0 R_D^3}{3RT\bar{I} \times (CE/100)},$$

where the period (τ) is determined by the detachment radius, the average current per cycle of oscillation ($\bar{I}$) and the collection efficiency of a single gas bubble (CE).

Surface tension change ratio calculation

The change in surface tension due to temperature gradients over a typical length scale L_T is given by

$$\Delta\sigma|_T = \sigma_T \frac{\partial T}{\partial s} L_T \approx \sigma_T \frac{\Delta T}{L_T} L_T = \sigma_T \Delta T,$$

where $\sigma_T = \partial\sigma/\partial T$ is the partial derivative of surface tension with T, $\partial T/\partial s$ is the gradient in the temperature field along the interface and ΔT is the total variation in temperature at the interface. Analogously, the difference in surface tension due to a change in the electrolyte concentration over a length L_C is given by

$$\Delta\sigma|_C = \sigma_C \frac{\partial C}{\partial s} L_C \approx \sigma_C \frac{\Delta C}{L_C} L_C = \sigma_C \Delta C.$$

The length scales (L_T and L_C) cancel for the estimates of $\Delta\sigma$, which then depend only on ΔT and ΔC, respectively. It is noteworthy, however, that there is a dependence on L for the resulting force on the bubble, for which $F \propto \Delta\sigma L$ if $R_D > L$. For purely diffusive growth, one expects $L_C \ll L_T$ given the much higher thermal diffusivity[52]. Yet, in the present case, additional mixing is likely to occur via the vigorous and frequent coalescence events and the Marangoni convection. Moreover, the reaction is running throughout the full cycle, whereas ohmic heating is most prevalent only at the end of the cycle when the electrode blockage is strongest[54]. Taken together, these factors suggest that the scale difference is less pronounced here, such that we expect comparable force magnitudes for similar $\Delta\sigma$ induced by thermal or solutal gradients.

ΔT was estimated by rescaling the reported values of ref. 27 (maximum $\Delta T \approx 14$ K at −2.95 mA) according to $\Delta T \propto I^2$ as implied by ohmic heating and using the average current levels at each potential (Fig. 5c).

Note that here we assume that the prefactor remains unchanged, which appears reasonable given the similarity of the configuration in ref. 27 (the same electrode size and similar bubble diameter). For ΔC, we used the upper limit value (1 mol l^{-1}), which is consistent with the rapid consumption of protons at the typically very high current densities achieved during the experiments (~−12.7 A cm^{-2} at −1 mA). The relative ratio between the estimated temperature and ion concentration contributions to the surface tension was plotted in Fig. 6 to evaluate the dominant driving of Marangoni convection.

Additionally, we note that the solutal Marangoni number

$$\mathrm{Ma_C} = \frac{\Delta\sigma_C R_D}{\mu D_C},$$

which relates the competing effects of Marangoni convection and diffusion, is always substantially larger than 1. The lowest value $\mathrm{Ma_C} \approx 1{,}800$ occurs for HCl at −0.11 V_{RHE}, indicating that even there Marangoni convection is relevant.

Data availability

All relevant data generated and analysed during this study are included in this article and its Supplementary Information. Data for the main figures are available in Zenodo (https://doi.org/10.5281/zenodo.7867261).

References

54. Hossain, S. S., Mutschke, G., Bashkatov, A. & Eckert, K. The thermocapillary effect on gas bubbles growing on electrodes of different sizes. *Electrochim. Acta* **353**, 136461 (2020).

Acknowledgements

This research received funding from the Dutch Research Council (NWO) in the framework of the ENW PPP Fund for the top sectors, from the Ministry of Economic Affairs in the framework of the PPS-toeslagregeling (grant number 741.019.201) and from the Advanced Research Center Chemical Building Blocks Consortium (ARC CBBC), under the project of New Chemistry for a Sustainable Future (project number 2021.038.C.UT.14). Additionally, the research is funded by Shell, Nobian and Nouryon. S.P. acknowledges the support by Basic Science Research Program through the National Research Foundation of Korea (NRF) funded by the Ministry of Education (2021R1A6A3A14039678). D.K., D.L. and M.T.M.K. received funding from the European Research Council (ERC) (BU-PACT grant agreement number 950111, ERC Advanced grant number 740479-DDD and ERC Advanced Grant 'FRUMKIN' number 101019998, respectively). We thank A. Bashkatov for insightful discussions on the subject.

Author contributions

S.P. and M.T.M.K. conceived the project. S.P., D.K. and M.T.M.K. designed the experiments. S.P. and O.v.d.H. carried out electrochemical characterization. S.P., L.L., Ç.D., D.L. and D.K. carried out bubble dynamics analysis. All authors read and commented on the manuscript. All authors approved the final version of the manuscript.

Competing interests

The authors declare no competing interests.

Additional information

Supplementary information The online version contains supplementary material available at https://doi.org/10.1038/s41557-023-01294-y.

Correspondence and requests for materials should be addressed to Dominik Krug or Marc T. M. Koper.

Peer review information *Nature Chemistry* thanks the anonymous reviewers for their contribution to the peer review of this work.